Journal of Power Sources 195 (2010) 5122–5129

Contents lists available at ScienceDirect

Journal of Power Sources

journal homepage: www.elsevier.com/locate/jpowsour

Evaluation on carbon nanocapsules for supercapacitors using a titanium cavity electrode

Cheng-Yeou Wu, Pu-Wei Wu*, Pang Lin

Department of Materials Science and Engineering, National Chiao Tung University Hsin-Chu 300, Taiwan

ARTICLE INFO

Article history:
Received 5 October 2009
Received in revised form 19 February 2010
Accepted 21 February 2010
Available online 1 March 2010

Keywords:
Carbon nanocapsules
Electrical double layer capacitor
Cavity electrode
Carbon blacks
Electrochemical analysis

ABSTRACT

We synthesize carbon nanocapsules (CNCs) by a flame combustion method and evaluate their potential as the electrode material for electrochemical double layer capacitor using a titanium cavity electrode (TCE). Identical process is conducted on commercially available carbonaceous materials such as Vulcan XC72R, Black Pearl 2000 (BP2000), multi-walled carbon nanotubes (MWCNTs), and active carbon (AC1100) for comparison purposes. Images from Scanning electron microscope and Transmission electron microscope on the CNCs demonstrate irregular-shaped particles in average size of 10–20 nm with graphene layers on perimeter compassing a hollow core. Electrochemical characterizations including cyclic voltammetry (CV), current reversal chronopotentiometry (CRC), and impedance spectroscopy are carried out in 1N H_2SO_4 to determine the specific capacitance and cycle life time. Among these samples, the BP2000 still delivers the highest specific capacitance in $F\,g^{-1}$ but the CNCs demonstrate the largest value in $\mu F\,cm^2$. In addition, the CNCs exhibit impressive life time for 5000 cycles without notable degradation. Consistent results are obtained by CV, CRC, and impedance measurements, validating the TCE as a facile tool to perform reliable electrochemical evaluations.

1. Introduction

Electrochemical supercapacitors have played a significant role in energy storage applications because their higher power density as opposed to conventional rechargeable batteries, longer energy storage duration over electrolytic capacitors, and in particular, theoretical infinite cycle life [1,2]. Hence, they are expected to be widely used in electrical vehicles and power tools to meet transient surge in power demand. Basing on the responsible mechanism for charge storage, the electrochemical supercapacitors are classified in two distinct categories; electrochemical double layer capacitors (EDLCs) and pseudocapacitors [1]. The EDLCs typically employ a carbon-based material with excessive surface area that enables the formation of double layer capacitance at the interface between the electrode and electrolyte [3]. Therefore, the surface area, porosity, pore size distribution, and surface functional group of the carbonaceous materials, as well as the type of electrolyte are critical in determining the resulting capacitance. In contrast, the pseudocapacitors entail a reversible faradaic reaction to store charge in different oxidation states using active materials such as metal oxides and conducting polymers [4]. Because a charge transfer reaction is involved, the pseudocapacitors usually exhibit a relatively larger capacitance as compared to that of EDLCs, albeit with a significant cost premium.

So far, a variety of carbonaceous materials have been investigated as the electrodes for EDLCs. They include active carbons, carbon blacks, carbon clothes, carbon fibers, carbon nanotubes, glassy carbons, and carbon aerogels [5–10]. Among them, the active carbons have attracted considerable attention because their desirable surface area and pore size distribution [3]. Recently, we demonstrate the rapid and large-quantity synthesis of carbon nanocapsules (CNCs) via an acetylene flame method, and report their impressive characteristics as the electrocatalyst supports for gas diffusion electrodes [11,12]. The as-synthesized CNCs reveal graphene layers on perimeters encompassing a hollow core and they can be considered as extremely short carbon nanotubes or fullerene nanoparticles. Since the graphene layers infer better electrical conductivity and the hollow core suggests reduced mass density, we surmise that the CNCs could be a possible candidate as the electrode materials for EDLCs.

The capacitive behaviors for an EDLC are extremely sensitive to both the electrode preparation process and measurement techniques [13,14]. To date, fabrications of porous composite electrode, thin film electrode (TFE), and cavity microelectrode (CME) are frequently adopted by many research groups for EDLCs evaluations [15–25]. Among them, the CME is known for facile determination on the intrinsic capacitance of interested materials since the addition of binder and conductive additive in the electrode fabrication process is not necessary. Moreover, the CME only requires

* Corresponding author. Tel.: +886 3 5131227; fax: +886 3 5724727.
E-mail address: ppwu@mail.nctu.edu.tw (P.-W. Wu).

0378-7753/$ – see front matter © 2010 Elsevier B.V. All rights reserved.
doi:10.1016/j.jpowsour.2010.02.053

a minute amount of active material so the inherent RC delay can be largely reduced. Unfortunately, the loading of CME is difficult to control as only a few micrograms of powders is used to fill the finite space in cavity. As a result, the exact determination of specific capacitance ($F g^{-1}$) becomes rather challenging. Therefore, a titanium cavity electrode (TCE) modified from the CME is designed and tested in this work. We recognize that the sample preparation steps for the TCE are much easier than those of CME and the active material (~mg) is nicely maintained in the cavity over the entire experiments.

In this work, the TCE is used to evaluate the CNCs for EDLCs applications. For comparison purposes, we also study commercially available carbonaceous materials including Vulcan XC72R (XC72R), Black Pearl 2000 (BP2000), multi-walled carbon nanotubes (MWCNTs), and active carbon (AC1100). Materials characterizations as well as electrochemical analysis including cyclic voltammetry (CV), current reversal chronopotentiometry (CRC), and impedance spectroscopy were performed.

2. Experimental

The CNCs were prepared by a flame combustion method using a mixture gas of C_2H_2 and O_2. They were formed in the incomplete combustion region of the flame and collected from the reaction chamber. Detailed synthetic setup and processing parameters were reported elsewhere [11,12,26]. The diameter for the as-synthesized CNCs was in the range of 10–20 nm. Afterward, the sample underwent a CO_2 treatment at 950 °C for 1 h to activate its surface. The XC72R (Cabot), BP2000 (Cabot), MWCNTs (Sigma–Aldrich), and AC1100 (Sigma–Aldrich) were used as received. Transmission electron microscope (TEM; JEOL JEM-2010) and Scanning electron microscope (SEM; Hitachi S4800) were employed to observe the microstructure and morphology of the CNCs. X-ray photoelectron spectroscope (Thermo Scientific K-Alpha) was adopted to identify the nature of functional groups on the carbon surface. BET surface area and associated pore size distribution were obtained by nitrogen adsorption and desorption (Micromeritics ASAP 2010).

The TCE, shown in Fig. 1, was made of a titanium rod in "J" shape with 2 mm of diameter and 200 mm in length. It contained a cylindrical cavity of 1 mm in diameter with 1 mm depth near the bottom. The surface of the TCE was coated with Teflon at 0.2 mm thickness. The sample to be studied was placed on a glass sheet and pressed compactly to fill the cavity. Since the titanium was electrochemically inactive under the testing conditions, the working electrode consisted of uncovered titanium metal and the pressed carbon material covered with a thin porous paper. The exact weight for the sample was measured with a microbalance at accuracy of 10 μg.

Electrochemical analysis was conducted in 1N H_2SO_4 solution at 26 °C in a three electrode cell consisting of Pt/Ti rod and Ag/AgCl as the counter and reference electrodes, respectively. Measurements including cyclic voltammetry, current reversal chronopotentiometry, and impedance spectroscopy were carried out using a Solarton 1281B potentiostat and a Solarton 1280 multiplexer. The CV was performed at scan rates of 5, 10, 20, 50, and 100 mV s^{-1} in potential windows of 0–0.6, 0–0.8, and 0–1 V, respectively. The CRC was performed with ±1 Ag^{-1} for identical potential ranges. The impedance spectra were obtained at the open circuit voltage with a sinusoidal signal of 10 mV for frequencies of 0.1–20 kHz. The recorded spectra were fitted by ZView® software to determine relevant parameters. Cyclic life time for the CNCs was estimated by repetitive CRC scans at ±1 Ag^{-1} within a potential window of 0–1 V.

To determine relevant contact angle and electrical resistance for the carbon materials under study, we also fabricated the TFEs via conventional lamination route. First, 0.9 g of sample and various amounts of polytetrafluoroethylene emulsion (Dupont, PTFE-30J 60 wt%) were mixed in 50 g of ethanol for 30 min to obtain a paste. Subsequently, the paste was pressed with a Ti mesh to form a TFE in 1 cm × 2 cm. The PTFE was used as a binder and its amount was adjusted between 5 and 15 wt% of the electrode weight. The contact angle was obtained by observing the H_2O droplet on the TFE (FACE CA-V150). Electrical resistance for the TFE was determined by a 4-point prob (Jiehan SRS4060).

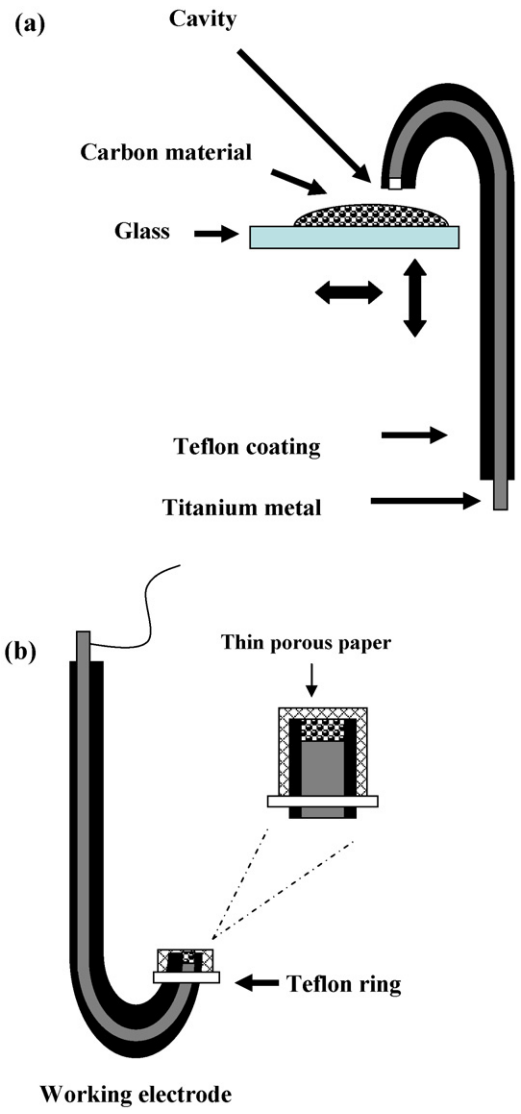

Fig. 1. A scheme diagram for TCE in (a) sample preparation and (b) electrochemical testing.

3. Results and discussion

Fig. 2(a) presents a high resolution TEM image for the as-synthesized CNCs before CO_2 treatment. As shown, the CNCs exhibited a core-shell microstructure consisting of approximate 10–20 co-axial graphene layers and an enclosed hollow core. Notably, some of the CNCs were connected to each other forming an aggregate in irregular shapes. The SEM image for the CNCs is demonstrated in Fig. 2(b). Apparently, the CNCs consisted of primary particles in uniform size of 10–20 nm and they formed a foam-like microstructure with numerous pores in between. Fig. 2(c) and (d) provide the CNCs images after CO_2 treatment. The CNCs maintained their original shapes but their sizes were

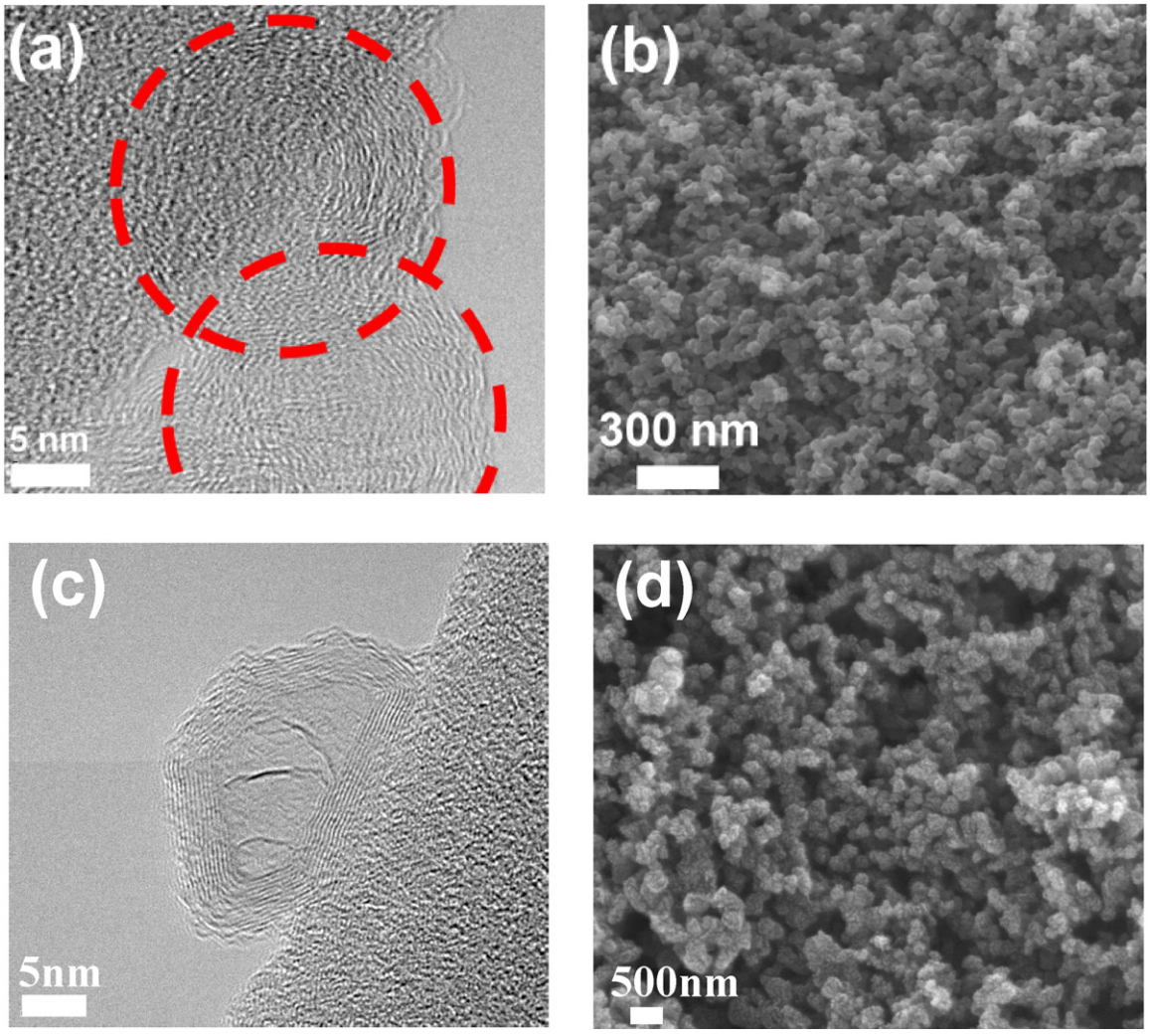

Fig. 2. Images for as-synthesized CNCs in (a) TEM and (b) SEM, as well as CNCs after CO_2 treatment in (c) TEM and (d) SEM.

slightly reduced. Notably there appeared moderate alteration on the graphene layers which was likely due to the localized CO_2 etching effect. Accordingly the CNCs BET surface area was increased from 299 to 471 $cm^2\ g^{-1}$ after CO_2 treatment.

In general, the pore size of a carbon material could be defined in three distinct classes; microspores (<2 nm), mesopores (2–50 nm), and macrospores (>50 nm). Their presence and relative amount could be estimated by N_2 adsorption and desorption isotherms which are provided in Fig. 3. Apparently, among our samples the AC1100 exhibited a type I behavior confirming its microporous nature. However, the remaining samples revealed a type IV pattern with the characteristic hysteresis behavior attributed to the presence of mesopores and their strong affinity to N_2. Relevant pore properties including total pore volume (V_{Pore}), micropore volume (V_{Micro}), BET surface area (S_{BET}), micropore surface area (S_{Micro}), external surface area (S_{Ext}), and average pore diameter (D_p) are listed in Table 1. From Table 1, the BP2000 demonstrated the highest pore volume and surface area while the XC72R revealed the least pore volume and surface area. Therefore, the XC72R is expected to deliver the lowest capacitance. In general, formation of macropores is conductive for ion diffusions so a larger EDLC is possible. However, an excessive large pore renders instability of EDLC which leads to a reduced specific capacitance. Hence, a suitable combination of macropores and mesopores is always desirable. From Table 1, the S_{Ext} ratio for the CNCs was similar to those of XC72R and BP2000, which confirmed the CNCs microstructures as shown in Fig. 2.

Fig. 4 displays the CV profiles for the CNCs in potential windows of 0–0.6, 0–0.8, and 0–1 V, respectively. We also measured the current response from an empty TCE for 0–1 V. As shown, the current recorded from the CNCs was at least 100 times greater

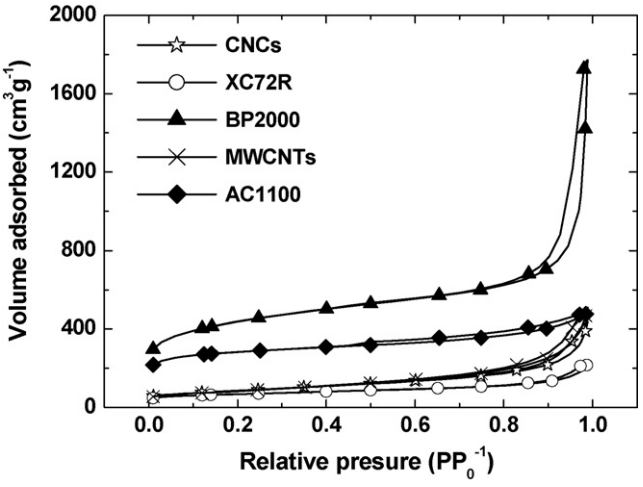

Fig. 3. N_2 adsorption and desorption isotherms for CNCs, XC72R, BP2000, MWCNTs, and AC1100, respectively.

Table 1
Relevant parameters for the pore properties determined by N_2 adsorption and desorption isotherms from CNCs, XC72R, BP2000, MWCNTs, and AC1100, respectively.

	CNCs	XC72R	BP2000	MWCNTs	AC1100
V_{Pore} ($cm^3\,g^{-1}$)	0.691	0.333	2.197	0.723	0.736
V_{Micro} ($cm^3\,g^{-1}$)	0.067	0.035	0.225	0.013	0.277
S_{BET}[a] ($m^2\,g^{-1}$)	471	238.7	1542	298.2	964.7
S_{Micro} ($m^2\,g^{-1}$)	148.7	76.7	505.5	32	597.7
S_{Ext}[b] ($m^2\,g^{-1}$)	322.3	162	1036.5	266.1	367
D_p (Å)	58.7	55.8	57	97	30.5
S_{Ext} ratio[c] (%)	68.4	67.9	67.2	89.2	38

[a] $S_{BET} = S_{Micro} + S_{Ext}$.
[b] S_{Ext} is the surface area including mesopores and macropores.
[c] S_{Ext} ratio $= S_{Ext}/S_{BET}$.

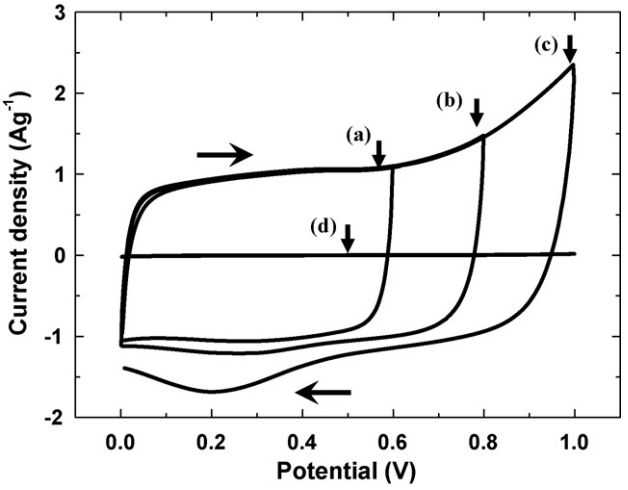

Fig. 4. CV profiles at 20 mV s^{-1} from CNCs in potential windows of (a) 0–0.6 V, (b) 0–0.8 V, (c) 0–1 V, and (d) empty TCE of 0–1 V, respectively.

than that of empty TCE, whose response appeared to be a straight line, suggesting possible current contribution from the titanium rod was negligible. At a potential window of 0–0.6 V, the CV curve was nearly rectangular. This indicated an ideal capacitive behavior from a polarizable electrode. However, once the potential window was extended to 0–0.8 V, an anodic current started to increase near 0.6 V, while a broad current response appeared between 0 and 0.4 V during cathodic scan. This behavior became more pronounced when the potential window was further raised to 0–1 V. According to literature, presence of these current peaks was attributed to the carbonyl and carboxyl functional groups that were formed during anodic scans and subsequently reduced in cathodic scans [27].

The specific capacitance could be determined from the CV profiles by the equation listed below,

$$C_S = \frac{Q}{w\Delta E} = \frac{\int i_c dt}{w\Delta E} \quad (1)$$

where C_S, Q, w, ΔE, and i_c are the specific capacitance ($F\,g^{-1}$), coulombs for discharge, weight of carbon, CV potential window, and cathodic current density, respectively. Values for the specific capacitance from Fig. 4 are provided in Table 2. For XC72R, its specific capacitance was estimated between 16 and 26 $F\,g^{-1}$. These

Table 2
Values of specific capacitance ($F\,g^{-1}$) calculated from CV profiles in various potential windows at 20 mV s^{-1} scan rate.

	CNCs	XC72R	BP2000	MWCNTs	AC1100
0–0.6 V	29.71	16.42	78.03	25.41	74.96
0–0.8 V	42.48	18.67	94.03	28.03	80.79
0–1 V	65.34	25.68	130.32	33.06	88

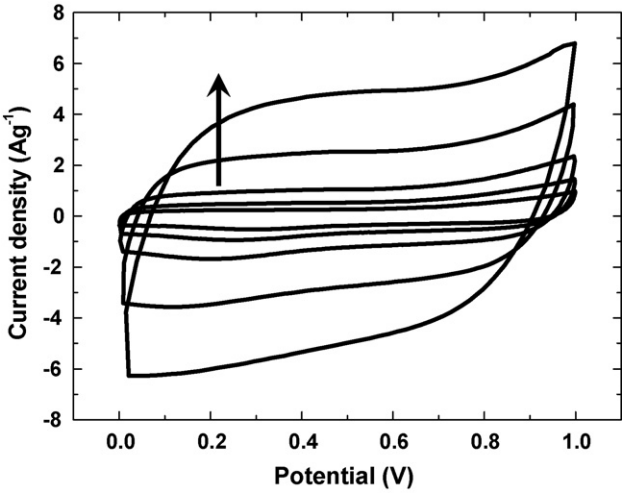

Fig. 5. CV profiles for CNCs at scan rates of 5, 10, 20, 50, and 100 mV s^{-1}, respectively.

values were consistent with what were reported earlier by Panic et al., as well as Centeno and Stoeckli using porous composite electrodes and TFEs in similar CV techniques [15,28]. This agreement substantiates the validity for the TCE to obtain specific capacitance accurately. Interestingly, the specific capacitance for the CNCs was in the range between 30 and 65 $F\,g^{-1}$, values that were above our expectation. Among these samples, the BP2000 still demonstrated the highest specific capacitance between 78 and 130 $F\,g^{-1}$ because of its excessive surface area. In contrast, the values for AC1100 were relatively insensitive to the potential windows and their values were between 75 and 88 $F\,g^{-1}$.

It is known that the specific capacitance of a porous electrode is also contingent on the scan rate imposed in the CV sweeps [29]. Fig. 5 demonstrates the CV profiles for the CNCs at different scan rates at potential window of 0–1 V. With an increasing scan rate, the current became larger correspondingly. In addition, there appeared a notable deviation from the ideal rectangular capacitive behavior. This distorted pattern is often attributed to the compromised ion diffusion within the micropores at sufficiently high scan rate. Identical process was also performed on XC72R, BP2000, MWCNTs, as well as AC1100, and their specific capacitances are presented in Table 3. As expected, for all these samples there were considerable reductions in the specific capacitance at high scan rates as compared to lower ones. For example, the specific capacitance of CNCs at 100 mV s^{-1} was 67% of what was obtained at 5 mV s^{-1}. Similarly, the XC72R, BP2000, MWCNTs, and AC1100 maintained 64, 39, 68, and 24% in identical situations. Notably, compared to BP2000 and AC1100, the CNCs suffered from the least capacitance loss at 100 mV s^{-1}.

An alternative approach to determine the specific capacitance is via the CRC technique. The CRC imposed an alternating current between the working and counter electrode in a predetermined potential window and recorded the resulting voltage variation with time. Since the CRC was carried out at fixed current, the specific

Table 3
Values of specific capacitance calculated from CV profiles at various scan rates in potential window of 0-1 V.

mV s^{-1}	CNCs	XC72R	BP2000	MWCNTs	AC1100
5 (a)	76.78	32.03	169.76	37.58	128.48
10	71.22	29.52	152.97	35.37	111.19
20	65.34	25.68	130.32	33.06	88
50	57.55	23.28	95.51	30.44	51.28
100 (b)	51.39	20.51	66.78	25.72	30.87
(b/a) (%)	66.93	64.03	39.34	68.44	24.03

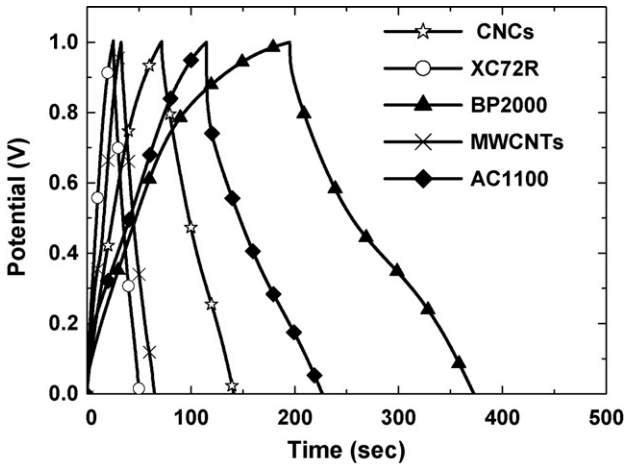

Fig. 6. CRC curves at ±1 Ag^{-1} in potential window of 0–1 V for CNCs, XC72R, BP2000, MWCNTs, and AC1100, respectively.

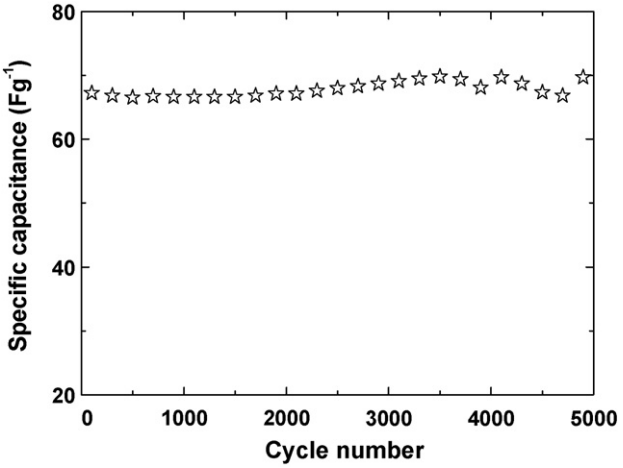

Fig. 7. Variation of specific capacitance for CNCs obtained from CRC measurements in potential window of 0–1 V at ±1 Ag^{-1} for 5000 cycles.

capacitance obtained was clearly defined. This is in sharp contrast with the specific capacitance derived from the CV method which was under a current-varying condition. In general, an ideal capacitor is expected to exhibit similar capacitance values from both CRC and CV approaches. Fig. 6 displays the voltage variation for our samples at a current density of ±1 Ag^{-1} for 0–1 V. Apparently, the recorded curves revealed a mirror-like symmetric pattern for CNCs, XC72R, and MWCNTs, which were indicative of ideal capacitive behaviors. In contrast, there appeared a slight distortion on both charging and discharging curves for BP2000 and AC1100, suggesting that moderate faradic reactions were likely to take place after 0.8 V. Additional information including the equivalent series resistance (ESR) could be derived from the CRC curves. The ESR is estimated by the sudden iR drop occurring when the applied current alters its polarity. The ESR is understood to include components such as the contact resistance between the electrode and current collector, the electrolyte resistance, as well as the intrinsic resistance of the active material. The average specific capacitance from the CRC method can be calculated using the equation below,

$$C_S = \frac{I}{w \times \left|\frac{dE}{dt}\right|} \approx \frac{Q}{w \times \Delta E} \quad (2)$$

where C_S, w, I, dE/dt, and Q are the specific capacitance ($F\,g^{-1}$), weight of carbon, current density for charge and discharge, slope for the discharge curves, and coulombs for discharge. Values for the specific capacitance and ESR are provided in Table 4. As listed, the iR drop for the CNCs and MWCNTs were substantially lower than those of XC72R, BP2000, and AC1100. This confirmed their conductive nature that we proposed earlier. Among these samples, the BP2000 and AC1100 still delivered rather high capacitance owing to their large intrinsic surface area.

To evaluate the life time for the CNCs, we carried out repetitive CRC experiments between 0 and 1 V at ±1 Ag^{-1}. The resulting capacitance for 5000 cycles is exhibited in Fig. 7. Apparently, the specific capacitance was nearly constant at 69 $F\,g^{-1}$ over the entire cycles. This is rather encouraging as the CNCs demonstrated desirable EDLC behaviors with impressive lifespan.

Impedance analysis is recognized as one of the principal methods examining fundamental behaviors of electrode materials for supercapacitors [1,15,30–34]. Fig. 8(a) demonstrates the Nyquist plots which reveal similar responses among our samples. The Nyquist plots were characterized by three distinct parts. At high frequency regime a semi-circle was observed, followed by a straight line with slope ca. 45° at intermediate frequency range. At the low frequency regime there appeared a vertical line. In general, the high frequency intercept at the Z' axis represents the sum of the resistances arising from the electrolyte, active material, and contact resistance between the active material and current collector.

Table 4
Relevant parameters determined from the CRC responses at ±1 Ag^{-1} in potential window of 0–1 V.

	CNCs	XC72R	BP2000	MWCNTs	AC1100
Q (C)	69.76	24.78	178	32.31	111.89
E^+ (V)	1	1	1	1	1
E^- (V)	0.974	0.965	0.964	0.979	0.885
iR drop (mV)	26	35	36	21	115
C_S ($F\,g^{-1}$)	71.62	25.68	184.6	33	126.4

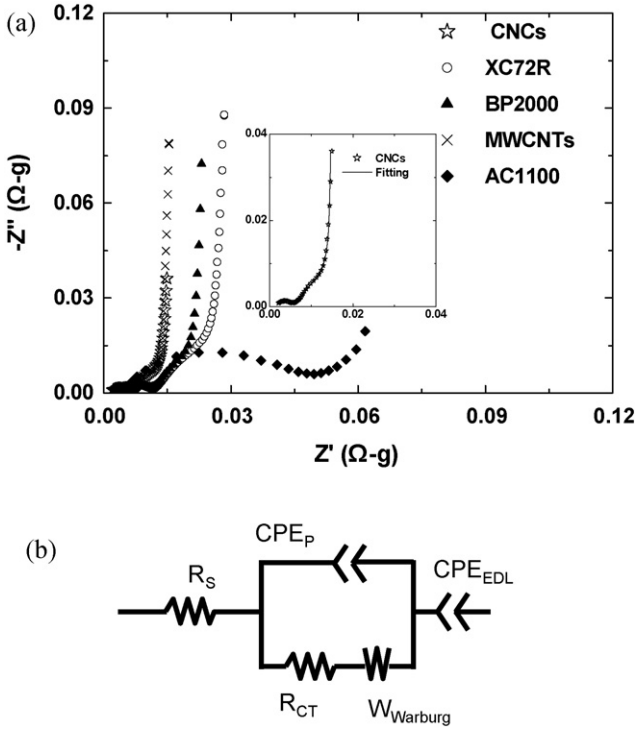

Fig. 8. (a) Nyquist plots for CNCs, XC72R, BP2000, MWCNTs, and AC1100 at the open circuit voltage in frequency range of 0.1–20 kHz, as well as (b) the equivalent circuit model used to fit the impedance spectra. Inset in (a) is the fitting of CNCs impedance spectrum.

Table 5
Parameters from fitting impedance spectra obtained OCP for CNCs, XC72R, BP2000, MWCNTs, and AC1100, respectively.

		CNCs	XC72R	BP2000	MWCNTs	AC1100
R_S ($\Omega\,g^{-1}$)		0.0014	0.0039	0.0021	0.0013	0.0046
CPE_P	T ($F\,g^{-1}$)	0.23	0.08	0.99	0.72	0.11
	q	0.69	0.72	0.50	0.56	0.72
R_{CT} ($\Omega\,g^{-1}$)		0.004	0.0075	0.0124	0.0048	0.0356
W	R ($\Omega\,g^{-1}$)	0.0096	0.0148	0.0063	0.0077	0.0376
	T ($F\,g^{-1}$)	0.44	0.29	0.62	0.16	12.33
	q	0.42	0.49	0.53	0.51	0.21
CPE_{EDL}	T ($F\,g^{-1}$)	45.62	18.12	82.85	20.2	101.3
	q	1	0.98	0.95	0.99	1

The semi-circle is associated with both faradic reaction and porous nature of the carbon electrode. The 45° straight line is attributed to the finite length diffusion from Warburg impedance. Response in the low frequency regime is expected to yield a vertical line, indicative of an ideal capacitive behavior from a polarizable electrode. Unfortunately, a slight deviation from the ideal 90° is often observed. This phenomenon is attributed to a dispersive pore size distribution on the electrode, which renders considerable penetration variation in alternative current signals [30].

The equivalent circuit model used to fit our impedance spectra is provided in Fig. 8(b). It involves several elements including R_S (ohmic resistance), R_{CT} (charge transfer resistance), CPE_P (constant phase element for charge transfer reaction), and CPE_{EDL} (constant phase element for electrochemical double layer). For both CPE_P and CPE_{EDL}, they can be represented by the following equation [35]:

$$Z = \frac{1}{T(j\omega)^q} \tag{3}$$

where Z, T, ω, and q are impedance, capacitance of associated element, angular frequency of the AC signal, and a variable between 0 and 1 for fitting purpose. For example, $q = 0$ indicates a pure resistor, and $q = 1$ represents an ideal parallel-plate capacitor. In between, the q infers an electrode with distinct porous structure [34].

Fitting of the impedance spectra for the CNCs is also shown in the inserted graph of Fig. 8(a) and relevant parameters from the fitting results are presented in Table 5 along with other samples. It is noted that the R_S value for CNCs was comparable to that of MWCNTs but lower than those of XC72R, BP2000, and AC1100. This confirmed the conductive nature of CNCs. The elements of CPE_p-T, W-T, and CPE_{EDL}-T represent the capacitive components of CPE_p, Warburg impedance, and CPE_{EDL}, respectively. For all these samples, the values of q for the CPE_p were below 1, which was expected for a typical porous electrode. Similarly, the q values for Warburg impedance were consistently under 1 because of limitations on ion diffusion in mesopores and micropores. Interestingly, both the CNCs and AC1100 showed CPE_{EDL} with q equals to 1. This demonstrated that the CNCs behaved similarly to AC1100 as an ideal capacitor.

Fig. 9 compares the specific capacitance derived from the CRC method along with values of micropore, external, and BET surface area for our samples. As shown, there appeared a general trend of increasing capacitance with BET surface area. Table 6 provides the specific capacitance and capacitance per unit area, based on

Table 6
Values of specific capacitance derived from the CRC responses and corresponding capacitance per unit area.

	CNCs	XC72R	BP2000	MWCNTs	AC1100
C_S ($F\,g^{-1}$)	71.62	25.68	184.6	33	126.4
C_{Ext} ($\mu F\,cm^{-2}$)	22.22	18.74	17.81	12.4	34.44
C_{BET} ($\mu F\,cm^{-2}$)	15.21	11.64	11.97	11.07	13.1

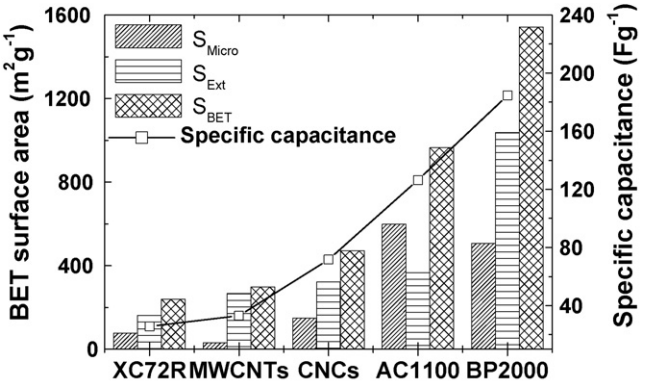

Fig. 9. Comparison in specific capacitance and surface area for CNCs, XC72R, BP2000, MWCNTs, and AC1100, respectively.

external surface area (C_{Ext}) and BET surface area (C_{BET}). As listed, the CNCs exhibited the highest value in C_{BET}. This inferred that the efficiency for surface usage of CNCs was significantly higher than others. Additionally, all our samples demonstrated values in the range of 11–16 $\mu F\,cm^{-2}$, which were in reasonable agreement with what was reported earlier by Frackowiak and Beguin [36]. Previously, Shi studied the specific capacitance of activated carbons and carbon fibers, and concluded that the contribution of micropores was relatively unchanged in the range of 15–20 $\mu F\,cm^{-2}$ [37]. In contrast, the amount of capacitance attributed to the mesopores and macropores were varied considerably depending on the type of carbons. However, following the methodology adopted by Shi in which the S_{Micro}/S_{Ext} was used in X-axis and C_S/S_{Ext} was used for Y-axis, we obtained a linear reaction ($y = 0.1419X + 0.1155$) for our samples. This indicated that the contribution to capacitance from micropores was 11.55 $\mu F\,cm^{-2}$, a value below what was suggested by Shi. This discrepancy might be resulted from the difference in the testing method.

It is established that certain surface attributes of carbons such as hydrophilicity and functional groups are critical in their capacitive behaviors. Fig. 10 presents the optical images for measurements on the contact angle on TFEs of CNCs, XC72R, BP2000, and MWCNTs. It is noted that the AC1100 failed to form a TFE in our lamination process and thus was unable to determine its contact angle. As shown, the BP2000 revealed the smallest contact angle while the CNCs behaved similarly to XC72R. As expected, the MWCNTs exhibited the largest contact angle for their hydrophobic nature. Electrical resistances on these TFEs via 4-point prob were also obtained. Their values were 3.245, 6.934, 3.384, and 2.715 $\Omega\,cm$ for the CNCs, XC72R, BP2000, and MWCNTs, respectively. Except MWCNTs, the CNCs demonstrated an enhanced electrical conductivity over XC72R and BP2000. This unique property, a fact that we established earlier in Table 4 for iR drop, was attributed to their aligned graphene layers on perimeters.

Fig. 11 provides the C_{1s} XPS profile for the CNCs and the curve fitting results are listed in Table 7. Apparently, the C_{1s} profile was composed of components labeled as C=C (carbon sp2 structure), C–C (carbon sp3 structure), C–OH, C=O, COOH, and aromatic ring

Table 7
The atomic ratios of C=C, C–C, C–OH, COOH, C=O, and aromatic ring for CNCs, XC72R, BP2000, MWCNTs, and AC1100, respectively.

	C=C	C–C	C–OH	COOH	C=O	Aromatic ring
CNCs	6.6	59.8	18.1	5.3	3.7	6.6
XC72R	5.3	62.6	16.9	3.5	5.7	6.1
BP2000	4.5	58.4	20.2	6.2	4.7	6.1
MWCNTs	5.2	61.4	19.7	3.8	3.2	6.9
AC1100	35.2	45.5	9.5	1.6	8.2	Not detectable

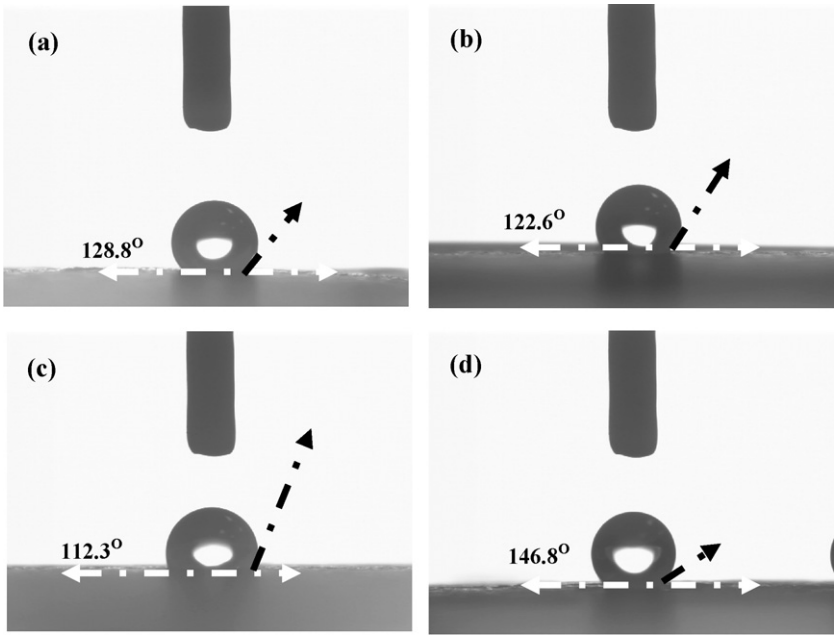

Fig. 10. Optical pictures in contact angle measurements for (a) CNCs, (b) XC72R, (c) BP2000, and (d) MWCNTs, respectively.

with individual peak positions determined at 284.5, 285.1, 286.2, 287.5, 289, and 291 eV, respectively [38–39]. According to Nian and Teng, the effect of surface functional groups on the capacitance was contingent on the type of functional groups [35]. For example, the C–OH and C=O were believed to increase the specific capacitance while the COOH behaved otherwise. From Table 7, the atomic ratios for the C–C and C=C in our samples were 63–81% with the principal functional group identified as C–OH. Except for the AC1100, which revealed a larger amount of C=O, there was no discernible difference among CNCs, XC72R, BP2000, and MWCNTs.

Our results so far indicate that the CNCs are desirable electrode materials for EDLC applications. As compared to other carbonaceous materials in this study, the CNCs provide suitable combinations of electrical conductivity, pore size distribution, and surface hydrophilicity. Moreover, one particular advantage of CNCs is their simple synthetic setup and processing that enables mass production at reduced cost.

To further demonstrate the validity and convenience of TCE over TFE, we carried out side-by-side comparisons in CVs and impedance measurements on CNCs. Fig. 12 provides the resulting CV profiles and impedance spectra from TCE, as well as TFEs with

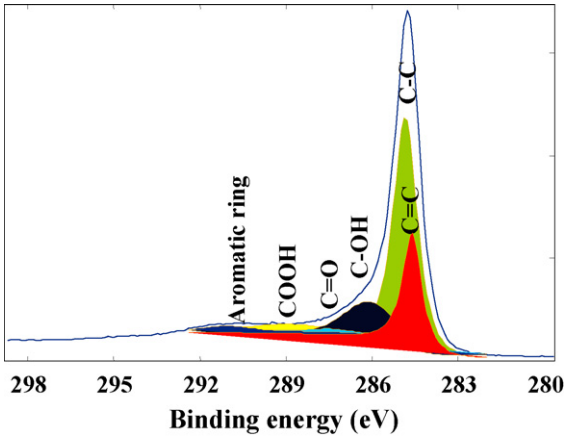

Fig. 11. C_{1s} XPS profile for CNCs.

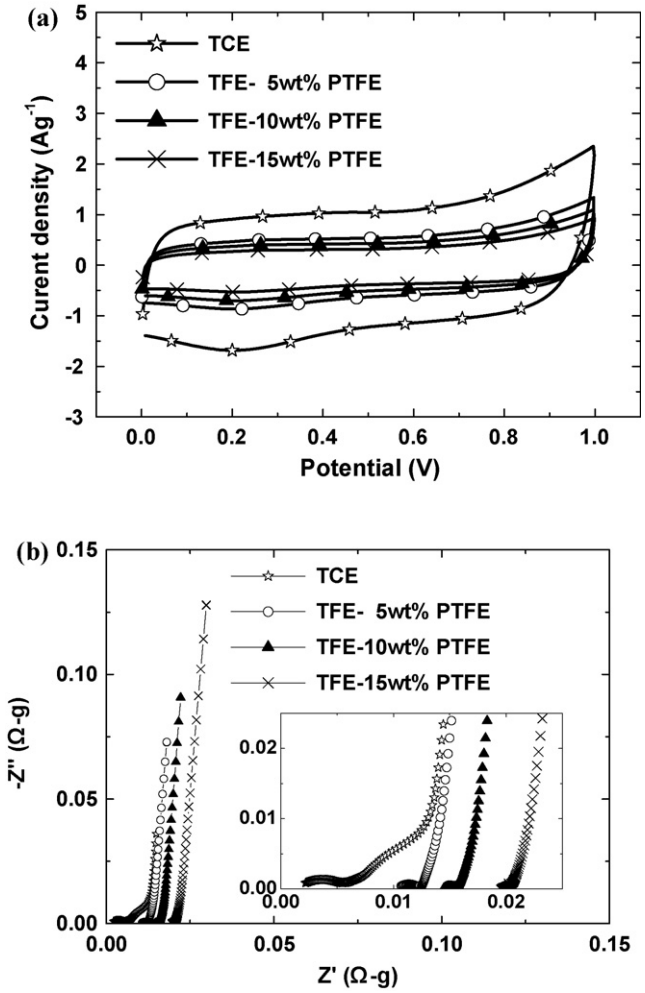

Fig. 12. Comparison of CNCs characteristics in (a) CV curves and (b) impedance spectra from TCE and TFEs with Teflon binder of 5, 10, and 15 wt%, respectively.

the addition of PTFE binder at 5, 10, and 15 wt%, respectively. As shown in Fig. 12(a), the resulting CV profiles were similar and the current densities were decreasing with increasing PTFE amounts. This pattern was caused by the passivation nature of PTFE that reduced the electrochemical active surface area effectively. With a moderate 5 wt% PTFE binder, the specific capacitance of TFE was largely reduced to only 54% of TCE. From the impedance spectra in Fig. 12(b), the addition of PTFE binder also shifted the impedance response to larger values. This trend suggested that the ESR and R_{CT} for the TFEs increased with increasing PTFE amount, a behavior that was not unexpected. From Fig. 12, it can be concluded that the TCE allows the accurate presentation of intrinsic materials properties on the capacitance behaviors without possible interference from PTFE binder. In addition, the TCE is particularly useful for carbon materials that are difficult to form TFE like AC1100. However, we would like to point out that since the TCE only requires an active loading in 100–500 μg, which is much larger than that of CME in a few micrograms, the TCE is not suitable to CV scans at extremely fast scan rate. Nevertheless, the TCE is capable of providing accurate reading on carbon materials for quick evaluations over conventional TFE.

4. Conclusions

We designed a TCE for quick evaluations on capacitive behaviors of CNCs. The CNCs were synthesized by a flame combustion approach followed by CO_2 treatment to activate their surface area. Images from SEM and TEM on the CNCs exhibited irregular-shaped particles in average size of 10–20 nm with graphene layers on perimeter encompassing a hollow core. Identical procedures were performed on the XC72R, BP2000, MWCNTs, and AC1100 for comparison purposes to validate the effectiveness of TCE. BET analysis revealed their surface area and pore size distribution in between XC72R and BP2000. The principal functional group on the CNCs surface was identified via XPS to be C–OH. Observation from contact angle revealed a similar behavior to that of XC72R but their electrical resistance was substantially reduced. Electrochemical characterizations including CV, CRC, and impedance spectroscopy were conducted to determine the specific capacitance and cyclic life time. Among these samples, the BP2000 delivered the highest specific capacitance in $F\,g^{-1}$ but the CNCs exhibited the largest value in $\mu F\,cm^2$. In addition, the CNCs displayed impressive cycle life without notable degradation. Consistent results were obtained by CV, CRC, and impedance measurements confirming the validity of TCE in electrochemical evaluations for EDLCs.

Acknowledgements

Equipment loan from the Taiwan Power Company is greatly appreciated. Assistance from Yun-Min Chang for manuscript preparation is noted.

References

[1] B.E. Conway, Electrochemical Supercapacitors, Kluwer–Plenum Press, New York, 1999.
[2] R. Kotz, M. Carlen, Electrochim. Acta 45 (2000) 2483–2498.
[3] A.G. Pandolfo, A.F. Hollenkamp, J. Power Sources 157 (2006) 11–27.
[4] P. Simon, Y. Gogotsi, Nat. Mater. 7 (2008) 845–854.
[5] W. Zhu, D.E. Miser, W.G. Chan, M.R. Hajaligol, Carbon 42 (2004) 1841–1845.
[6] J. Niu, W.G. Pell, B.E. Conway, J. Power Sources 156 (2006) 725–740.
[7] B.O. Boskovic, V.B. Golovko, M. Cantoro, B. Kleinsorge, A.T.H. Chuang, C. Ducati, S. Hofmann, J. Robertson, B.F.G. Johnson, Carbon 43 (2005) 2643–2648.
[8] D. Tashima, K. Kurosawatsu, M. Uota, T. Karashima, M. Otsubo, C. Honda, Y.M. Sung, Thin Solid Films 515 (2007) 4234–4239.
[9] D. Sun, L. Zhu, G. Zhu, Anal. Chim. Acta 564 (2006) 243–247.
[10] J.M. Miller, B. Dunn, Langmuir 15 (1999) 799–806.
[11] C.Y. Wu, P.W. Wu, P. Lin, Y.Y. Li, Y.M. Lin, J. Electrochem. Soc. 154 (2007) B1059–B1062.
[12] Y.M. Lin, Y.M. Chang, P.W. Wu, P. Lin, Y.Y. Li, C.Y. Wu, C.F. Tsai, K.Y. Yeh, J. Appl. Electrochem. 38 (2008) 507–514.
[13] C.C. Hu, W.C. Chen, Electrochim. Acta 49 (2004) 3469–3477.
[14] W.C. Chen, C.C. Hu, C.C. Wang, C.K. Min, J. Power Sources 125 (2004) 292–298.
[15] V.V. Panic, R.M. Stevanovic, V.M. Jovanovic, A.B. Dekanski, J. Power Sources 181 (2008) 186–192.
[16] C. Xu, B. Li, H. Du, F. Kang, Y. Zeng, J. Power Sources 180 (2008) 664–670.
[17] X. Liu, P.G. Pickup, J. Power Sources 176 (2008) 410–416.
[18] E. Machefaux, T. Brousse, D. Belanger, D. Guyomard, J. Power Sources 165 (2007) 651–655.
[19] C.W. Huang, Y.T. Wu, C.C. Hu, Y.Y. Li, J. Power Sources 172 (2007) 460–467.
[20] C.C. Hu, C.C. Wang, K.H. Chang, Electrochim. Acta 52 (2007) 2691–2700.
[21] V. Vivier, C. Cachet-Vivier, C.S. Cha, J.Y. Nedelec, L.T. Yu, Electrochem. Commun. 2 (2000) 180–185.
[22] V. Vivier, C. Cachet-Vivier, B.L. Wu, C.S. Cha, J.Y. Nedelec, L.T. Yu, Electrochem. Solid State Lett. 2 (1999) 385–387.
[23] V. Vivier, C. Cachet-Vivier, D. Michel, J.Y. Nedelec, L.T. Yu, Synth. Met. 126 (2002) 253–262.
[24] C. Cachet-Vivier, V. Vivier, C.S. Cha, J.Y. Nedelec, L.T. Yu, Electrochim. Acta 47 (2001) 181–189.
[25] C. Portet, J. Chmiola, Y. Gogotsi, S. Park, K. Lian, Electrochim. Acta 53 (2008) 7675–7680.
[26] T.C. Liu, Y.Y. Li, Carbon 44 (2006) 2045–2050.
[27] M.G. Sullivan, R. Kotz, O. Haas, J. Electrochem. Soc. 147 (2000) 308–317.
[28] T.A. Centeno, F. Stoeckli, Electrochim. Acta 52 (2006) 560–566.
[29] S. Ardizzone, G. Fregonara, S. Trasatti, Electrochim. Acta 35 (1990) 263–267.
[30] J. Gamby, P.L. Taberna, P. Simon, J.F. Fauvarque, M. Chesneau, J. Power Sources 101 (2001) 109–116.
[31] M. Toupin, D. Belanger, I.R. Hill, D. Quinn, J. Power Sources 140 (2005) 203–210.
[32] L. Bonnefoi, P. Simon, J.F. Fauvarque, C. Sarrazin, J.F. Sarrau, A. Dugast, J. Power Sources 80 (1999) 149–155.
[33] D. Qu, J. Power Sources 109 (2002) 403–411.
[34] H.K. Song, H.Y. Hwang, K.H. Lee, L.H. Dao, Electrochim. Acta 45 (2000) 2241–2257.
[35] Y.R. Nian, H. Teng, J. Electroanal. Chem. 540 (2003) 119–127.
[36] E. Frackowiak, F. Beguin, Carbon 39 (2001) 937–950.
[37] H. Shi, Electrochim. Acta 41 (1996) 1633–1639.
[38] Z.R. Yue, W. Jiang, L. Wang, S.D. Gardner, J.C.U. Pittman, Carbon 37 (1999) 1785–1796.
[39] J. Lahaye, Fuel 77 (1998) 543–547.